Biomedical Optics EXPRESS

Wide-field *in vivo* oral OCT imaging

Anthony M. D. Lee,[1,*] Lucas Cahill,[1] Kelly Liu,[1] Calum MacAulay,[1] Catherine Poh,[1,2] and Pierre Lane[1]

[1]*Department of Integrative Oncology - Cancer Imaging Unit, British Columbia Cancer Research Centre, Vancouver, BC, V5Z 1L3, Canada*
[2]*Faculty of Dentistry, University of British Columbia, Vancouver, BC, V6T 1Z3, Canada*
[*]*alee@bccrc.ca*

Abstract: We have built a polarization-sensitive swept source Optical Coherence Tomography (OCT) instrument capable of wide-field *in vivo* imaging in the oral cavity. This instrument uses a hand-held side-looking fiber-optic rotary pullback catheter that can cover two dimensional tissue imaging fields approximately 2.5 mm wide by up to 90 mm length in a single image acquisition. The catheter spins at 100 Hz with pullback speeds up to 15 mm/s allowing imaging of areas up to 225 mm^2 field-of-view in seconds. A catheter sheath and two optional catheter sheath holders have been designed to allow imaging at all locations within the oral cavity. Image quality of 2-dimensional image slices through the data can be greatly enhanced by averaging over the orthogonal dimension to reduce speckle. Initial *in vivo* imaging results reveal a wide-field view of features such as epithelial thickness and continuity of the basement membrane that may be useful in clinic for chair-side management of oral lesions.

OCIS codes: (170.4500) Optical coherence tomography; (170.3890) Medical optics instrumentation; (170.4580) Optical diagnostics for medicine; (170.1610) Clinical applications; (170.1850) Dentistry; (170.4940) Otolaryngology.

References and links

1. S. I. J. Ferlay, M. Ervik, R. Dikshit, S. Eser, C. Mathers, M. Rebelo, D. M. Parkin, D. Forman, and F. Bray, "GLOBOCAN 2012 v1.0, Cancer Incidence and Mortality Worldwide: IARC CancerBase No. 11 " (International Agency for Research on Cancer, 2013), retrieved http://globocan.iarc.fr, accessed on Jan. 5, 2015.
2. J. M. Zakrzewska, "Fortnightly review: Oral cancer," BMJ **318**(7190), 1051–1054 (1999).
3. C. Scully and S. Porter, "ABC of oral health. Oral cancer," BMJ **321**(7253), 97–100 (2000).
4. J. Pindborg, P. Reichart, C. Smith, and I. van der Wall, Histological Typing of Cancer and Precancer of the Oral Mucosa (Springer Berlin Heidelberg, 1997).
5. P. Wilder-Smith, J. Holtzman, J. Epstein, and A. Le, "Optical diagnostics in the oral cavity: an overview," Oral Dis. **16**(8), 717–728 (2010).
6. M.-T. Tsai, H.-C. Lee, C.-K. Lee, C.-H. Yu, H.-M. Chen, C.-P. Chiang, C.-C. Chang, Y.-M. Wang, and C. C. Yang, "Effective indicators for diagnosis of oral cancer using optical coherence tomography," Opt. Express **16**(20), 15847–15862 (2008).
7. W. Jerjes, T. Upile, B. Conn, Z. Hamdoon, C. S. Betz, G. McKenzie, H. Radhi, M. Vourvachis, M. El Maaytah, A. Sandison, A. Jay, and C. Hopper, "In vitro examination of suspicious oral lesions using optical coherence tomography," Br. J. Oral Maxillofac. Surg. **48**(1), 18–25 (2010).
8. Z. Hamdoon, W. Jerjes, R. Al-Delayme, G. McKenzie, A. Jay, and C. Hopper, "Structural validation of oral mucosal tissue using optical coherence tomography," Head Neck Oncol. **4**(1), 29 (2012).
9. Z. Hamdoon, W. Jerjes, T. Upile, G. McKenzie, A. Jay, and C. Hopper, "Optical coherence tomography in the assessment of suspicious oral lesions: An immediate ex vivo study," Photodiagn. Photodyn. Ther. **10**(1), 17–27 (2013).
10. O. K. Adegun, P. H. Tomlins, E. Hagi-Pavli, G. McKenzie, K. Piper, D. L. Bader, and F. Fortune, "Quantitative analysis of optical coherence tomography and histopathology images of normal and dysplastic oral mucosal tissues," Lasers Med. Sci. **27**(4), 795–804 (2012).
11. V. Volgger, H. Stepp, S. Ihrler, M. Kraft, A. Leunig, P. M. Patel, M. Susarla, K. Jackson, and C. S. Betz, "Evaluation of optical coherence tomography to discriminate lesions of the upper aerodigestive tract," Head Neck **35**(11), 1558–1566 (2013).
12. S. Prestin, S. I. Rothschild, C. S. Betz, and M. Kraft, "Measurement of epithelial thickness within the oral cavity using optical coherence tomography," Head Neck **34**(12), 1777–1781 (2012).

#236612 Received 20 Mar 2015; revised 18 Jun 2015; accepted 19 Jun 2015; published 24 Jun 2015

13. J. M. Ridgway, W. B. Armstrong, S. Guo, U. Mahmood, J. Su, R. P. Jackson, T. Shibuya, R. L. Crumley, M. Gu, Z. Chen, and B. J. Wong, "In vivo optical coherence tomography of the human oral cavity and oropharynx," Arch. Otolaryngol. Head Neck Surg. **132**(10), 1074–1081 (2006).
14. P. Wilder-Smith, W.-G. Jung, M. Brenner, K. Osann, H. Beydoun, D. Messadi, and Z. Chen, "In vivo optical coherence tomography for the diagnosis of oral malignancy," Lasers Surg. Med. **35**(4), 269–275 (2004).
15. M.-T. Tsai, H.-M. Chen, Y.-M. Wang, C.-C. Yang, C.-P. Chiang, C.-K. Lee, and H.-C. Lee, "Differentiating oral lesions in different carcinogenesis stages with optical coherence tomography," J. Biomed. Opt. **14**, 044028 (2009).
16. C.-K. Lee, T.-T. Chi, C.-T. Wu, M.-T. Tsai, C.-P. Chiang, and C.-C. Yang, "Diagnosis of oral precancer with optical coherence tomography," Biomed. Opt. Express **3**(7), 1632–1646 (2012).
17. B. Davoudi, A. Lindenmaier, B. A. Standish, G. Allo, K. Bizheva, and A. Vitkin, "Noninvasive in vivo structural and vascular imaging of human oral tissues with spectral domain optical coherence tomography," Biomed. Opt. Express **3**(5), 826–839 (2012).
18. W. J. Choi and R. K. Wang, "In vivo imaging of functional microvasculature within tissue beds of oral and nasal cavities by swept-source optical coherence tomography with a forward/side-viewing probe," Biomed. Opt. Express **5**(8), 2620–2634 (2014).
19. Y. Yoon, W. H. Jang, P. Xiao, B. Kim, T. Wang, Q. Li, J. Y. Lee, E. Chung, and K. H. Kim, "In vivo wide-field reflectance/fluorescence imaging and polarization-sensitive optical coherence tomography of human oral cavity with a forward-viewing probe," Biomed. Opt. Express **6**(2), 524–535 (2015).
20. B. J. F. Wong, R. P. Jackson, S. Guo, J. M. Ridgway, U. Mahmood, J. Su, T. Y. Shibuya, R. L. Crumley, M. Gu, W. B. Armstrong, and Z. Chen, "In Vivo Optical Coherence Tomography of the Human Larynx: Normative and Benign Pathology in 82 Patients," Laryngoscope **115**(11), 1904–1911 (2005).
21. M.-T. Tsai, C.-P. Chiang, H.-C. Lee, C.-W. Lu, Y.-M. Wang, C.-K. Lee, and C. C. Yang, "Delineation of an oral cancer lesion with swept-source optical coherence tomography," J. Biomed. Opt. **13**, 044012 (2008).
22. N. Ozawa, Y. Sumi, C. Chong, and T. Kurabayashi, "Evaluation of oral vascular anomalies using optical coherence tomography," Br. J. Oral Maxillofac. Surg. **47**(8), 622–626 (2009).
23. N. Ozawa, Y. Sumi, K. Shimozato, C. Chong, and T. Kurabayashi, "In vivo imaging of human labial glands using advanced optical coherence tomography," Oral Surg. Oral Med. Oral Pathol. Oral Radiol. Endod. **108**(3), 425–429 (2009).
24. D. Wang, L. Fu, X. Wang, Z. Gong, S. Samuelson, C. Duan, H. Jia, J. S. Ma, and H. Xie, "Endoscopic swept-source optical coherence tomography based on a two-axis microelectromechanical system mirror," J. Biomed. Opt. **18**(8), 086005 (2013).
25. L. M. Higgins and M. C. Pierce, "Design and characterization of a handheld multimodal imaging device for the assessment of oral epithelial lesions," J. Biomed. Opt. **19**(8), 086004 (2014).
26. I.-K. Jang, G. J. Tearney, B. MacNeill, M. Takano, F. Moselewski, N. Iftima, M. Shishkov, S. Houser, H. T. Aretz, E. F. Halpern, and B. E. Bouma, "In Vivo Characterization of Coronary Atherosclerotic Plaque by Use of Optical Coherence Tomography," Circulation **111**(12), 1551–1555 (2005).
27. D. C. Adler, C. Zhou, T.-H. Tsai, J. Schmitt, Q. Huang, H. Mashimo, and J. G. Fujimoto, "Three-dimensional endomicroscopy of the human colon using optical coherence tomography," Opt. Express **17**(2), 784–796 (2009).
28. M. J. Suter, P. A. Jillella, B. J. Vakoc, E. F. Halpern, M. Mino-Kenudson, G. Y. Lauwers, B. E. Bouma, N. S. Nishioka, and G. J. Tearney, "Image-guided biopsy in the esophagus through comprehensive optical frequency domain imaging and laser marking: a study in living swine," Gastrointest. Endosc. **71**(2), 346–353 (2010).
29. A. M. D. Lee, K. Ohtani, C. Macaulay, A. McWilliams, T. Shaipanich, V. X. D. Yang, S. Lam, and P. Lane, "In vivo lung microvasculature visualized in three dimensions using fiber-optic color Doppler optical coherence tomography," J. Biomed. Opt. **18**(5), 050501 (2013).
30. A. M. D. Lee, H. Pahlevaninezhad, V. X. D. Yang, S. Lam, C. MacAulay, and P. Lane, "Fiber-optic polarization diversity detection for rotary probe optical coherence tomography," Opt. Lett. **39**(12), 3638–3641 (2014).
31. Z. Wang, H.-C. Lee, O. O. Ahsen, B. Lee, W. Choi, B. Potsaid, J. Liu, V. Jayaraman, A. Cable, M. F. Kraus, K. Liang, J. Hornegger, and J. G. Fujimoto, "Depth-encoded all-fiber swept source polarization sensitive OCT," Biomed. Opt. Express **5**(9), 2931–2949 (2014).
32. L. Cahill, A. M. D. Lee, H. Pahlevaninezhad, S. Ng, C. E. MacAulay, C. Poh, and P. Lane, "Passive endoscopic polarization sensitive optical coherence tomography with completely fiber based optical components," Proc. SPIE **9304**, 930413 (2015).
33. P. Wilder-Smith, K. Lee, S. Guo, J. Zhang, K. Osann, Z. Chen, and D. Messadi, "In vivo diagnosis of oral dysplasia and malignancy using optical coherence tomography: Preliminary studies in 50 patients," Lasers Surg. Med. **41**(5), 353–357 (2009).
34. C. F. Poh, L. Zhang, D. W. Anderson, J. S. Durham, P. M. Williams, R. W. Priddy, K. W. Berean, S. Ng, O. L. Tseng, C. MacAulay, and M. P. Rosin, "Fluorescence Visualization Detection of Field Alterations in Tumor Margins of Oral Cancer Patients," Clin. Cancer Res. **12**(22), 6716–6722 (2006).
35. J. F. de Boer, T. E. Milner, M. J. C. van Gemert, and J. S. Nelson, "Two-dimensional birefringence imaging in biological tissue by polarization-sensitive optical coherence tomography," Opt. Lett. **22**(12), 934–936 (1997).
36. E. Z. Zhang, W.-Y. Oh, M. L. Villiger, L. Chen, B. E. Bouma, and B. J. Vakoc, "Numerical compensation of system polarization mode dispersion in polarization-sensitive optical coherence tomography," Opt. Express **21**(1), 1163–1180 (2013).
37. B. Park, M. Pierce, B. Cense, and J. de Boer, "Real-time multi-functional optical coherence tomography," Opt. Express **11**(7), 782–793 (2003).

#236612 Received 20 Mar 2015; revised 18 Jun 2015; accepted 19 Jun 2015; published 24 Jun 2015

1. Introduction

Worldwide in 2015, it is estimated that there will be over 325,000 new cases of, and over 157,000 deaths attributable to oral and lip cancer [1], with the majority of these being squamous cell carcinoma [2, 3]. Histologically, key indicators of squamous epithelial dysplasia include increased nuclear-cytoplasmic ratio, irregular epithelial stratification and bulbous rete ridges [4], while destruction of the basement membrane indicates invasive cancer. Immediate or real-time clinical imaging of these tissue features in the oral cavity may have useful applications for cancer detection and management. In the former, *in vivo* imaging of large suspicious oral lesions may indicate whether biopsy is necessary or guide clinicians to the sites that are most diagnostically useful. In the latter, *in vivo* imaging may potentially provide real-time information of lesion extension to better delineate surgical boundaries, and subsequently reduce disease recurrence by facilitating entire tumour resection.

Optical coherence tomography (OCT) is an optical imaging technique that has shown promise for oral cancer detection and diagnosis [5]. *Ex vivo* studies have reported the ability of OCT to define cancer boundaries [6], and measure changes in tissue features associated with oral cancer diagnosis such as the thicknesses of the keratin layer, epithelial layer, and lamina propria, as well as identify the continuity of the basement membrane [7–9]. Quantitative analysis of the OCT attenuation coefficient in the epithelial layer of formalin-fixed biopsy specimens has been employed to discriminate normal from mild, moderate and severe dysplasia with some success [10]. Several groups have performed *in vivo* oral cavity imaging to quantify epithelial thickness at different sites around the oral cavity [11, 12], and identify tissue layers and microstructures [13]. A scoring system based on tissue changes and features read from OCT images showed good agreement of diagnoses ranging from normal to SCC between trained observers and histopathology [14]. Automated image analysis algorithms have also been developed to separate moderate dysplasia from mild dysplasia with 82% sensitivity and 90% specificity [15, 16]. Vasculature in the oral cavity has also been imaged using Doppler OCT, speckle variance OCT [17], and optical micro-angiography [18]. Polarization-sensitive OCT has also been combined with fluorescence imaging of the oral mucosa [19].

While many OCT systems and *in vivo* scanners have been reported for the oral cavity, most if not all of these systems lack sufficient field-of-view and flexibility to make them an effective and efficient tool in clinical practice. An adjunctive imaging device for biopsy or surgical guidance must 1) reach all areas of the oral cavity where lesions may be located; 2) scan a field-of-view (FOV) that is sufficiently wide to cover extensive lesions; 3) scan rapidly to mitigate patient and clinician motion artifacts; and 4) provide imaging in a practical time frame. To our knowledge, a commercial OCT system designed specifically for the oral cavity is not currently available. The general purpose Imalux Niris Imaging System with its small diameter catheter has been used by a number of researchers for *in vivo* studies in the oral cavity. Its fiber-based catheter allows flexible placement within the oral cavity [11, 12, 14], however, its 1-D scanner covering only 2mm at a time makes it impossible to image large areas of the oral cavity in a timely fashion. Custom designed probes using linear scanners and distal tip optics to direct the beam perpendicular to the fiber axis allowing scans up to approximately 10 mm in length have been reported, however, they have no ability to scan in two dimensions and the scan speeds are slow for *in vivo* imaging [20, 21]. A number of groups have presented 2-D galvanometer- or MEMS-scanned systems but they also have small FOV and/or large scan heads that limit versatile positioning in the oral cavity [17–19, 22–25].

In this work, we present an OCT system and rotary-pullback catheter (RPC) for imaging in the oral cavity. RPC designs have been used in cardiology [26], gastroenterology [27, 28], and pulmonology [29]. RPCs have distal optics that focus and direct light perpendicular to a spinning fiber axis to generate circular OCT images. Retracting the fiber while it spins, called a pullback, creates a helical scan pattern that produces full 3-D volumetric imaging. The rotary and pullback motions of our catheter are up to 100 Hz and millimeters per second,

#236612 Received 20 Mar 2015; revised 18 Jun 2015; accepted 19 Jun 2015; published 24 Jun 2015

respectively, resulting in very fast 3-D imaging over large areas. Averaging along the different imaging axes provides high quality OCT images with greatly reduced speckle. We present catheter sheaths and holders that allow placement of the RPC in almost any location within the oral cavity. In addition to demonstrating wide-field structural imaging, we also demonstrate wide-field polarization sensitive OCT (PSOCT) imaging.

2. Materials and methods

2.1 OCT imaging system

The polarization-sensitive swept-source OCT system is shown in Fig. 1. It is based on a polarization-diversity detection OCT system described previously [30]. Briefly, a 50.4 kHz swept source laser (SSOCT-1310, Axsun Technologies Inc., Billerica, MA) with approximately 20 mW polarized output power centered at 1310 nm and 100 nm bandwidth (FWHM) is coupled 90% sample/10% reference into a single-mode Mach-Zehnder OCT interferometer. Polarization controllers allow adjustment of the laser polarization prior to entry into the sample and reference optical circulators when the interferometer is being operated in polarization-independent OCT imaging mode. A polarization-maintaining (PM) patch cord and length-matched single-mode (SM) patch cord can be inserted before the reference and sample circulators respectively to enable depth-encoded PSOCT as demonstrated by Wang *et al.* [31]. The length of the PM and SM patch cables were chosen to be 12 m, providing a depth separation of 2.33 mm in air (1.66 mm in tissue) between the two polarization states in the OCT images. The sample arm consists of a fiber optic rotary joint (FORJ, MJP-SAPB, Princetel Inc; Pennington, NJ) connected to a 0.9 mm outer diameter (OD), rotary-pullback catheter (RPC, C7 Dragonfly Imaging Catheter, St. Jude Medical Inc, St. Paul, MN). Insertion losses through the FORJ and RPC are 1.99dB and 2.14dB respectively, resulting in approximately 5mW of power incident upon the tissue. A custom built motor assembly allows rotational and pullback imaging capability. A 660 nm diode laser (S1FC660, Thorlabs Inc., Newton, NJ) is coupled into the sample arm using a wavelength division multiplexer (WD202A2, Thorlabs) to allow visualization of the imaging location on the tissue.

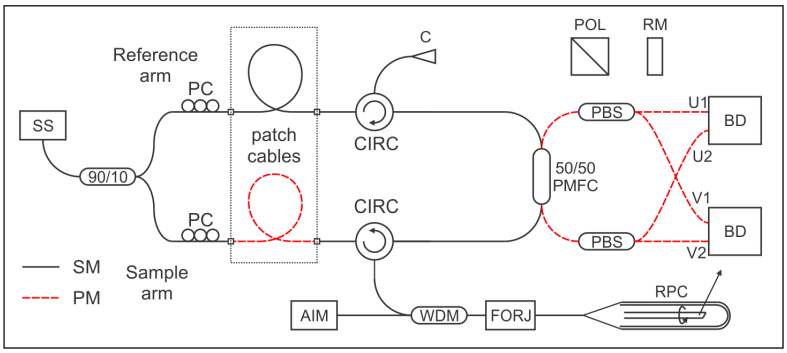

Fig. 1. Schematic diagram of endoscopic PSOCT system. SS = swept-source laser, PC = polarization controller, CIRC = circulator, C = collimator, POL = polarizer, RM = reference mirror, AIM = aiming laser, WDM = wavelength division multiplexer, FORJ = fiber optic rotary joint, RPC = rotary pullback catheter, PMFC = polarization maintaining fiber coupler, PBS = polarization beamsplitter, BD = balanced detector. Dashed (red) lines indicate PM fiber; all others are SM fiber. The SM and PM patch cables indicated within the dotted box can be removed to yield a standard (polarization-independent) OCT imaging system.

A thin-film polarizer mounted in a rotational stage is inserted before the reference arm mirror to balance the reference polarization powers at the detectors as described previously [30]. Light returning from the sample and reference arms are combined by a 50/50 polarization independent coupler with SM fiber inputs and PM fiber outputs that are spliced to polarization beam splitters (PBS). Polarization matched outputs from the PBS's are connected

#236612 Received 20 Mar 2015; revised 18 Jun 2015; accepted 19 Jun 2015; published 24 Jun 2015

to 75 MHz balanced detectors (PDB420C, Thorlabs) constituting the X and Y detection channels. A high-speed digitizer (ATS9350, Alazar Technologies Inc., Pointe-Claire, QC) in 'k-clock' acquisition mode collects the data. Custom data acquisition software provides real time 2-D OCT image display.

2.2 In vivo imaging

In vivo OCT imaging of the oral cavity was approved by the Research Ethics Board of the University of British Columbia and the British Columbia Cancer Agency (H11-02516).

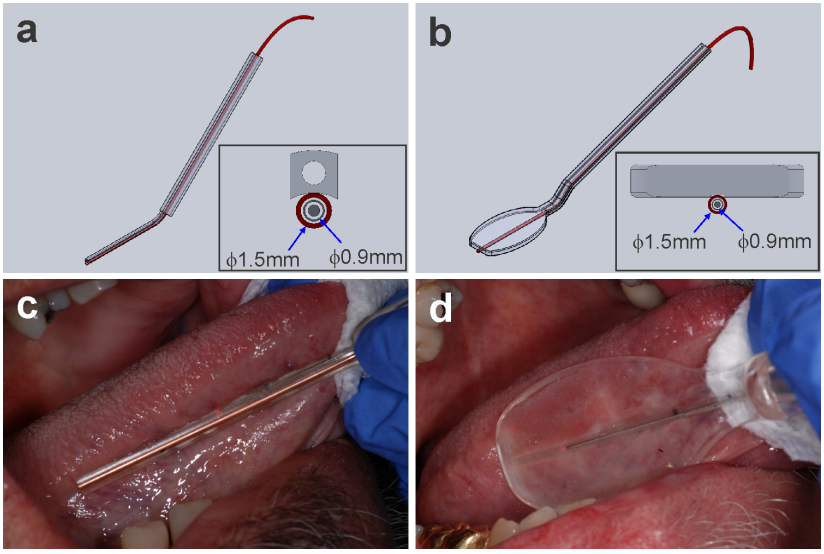

Fig. 2. Fiber optic OCT catheter holders for oral imaging. Catheter sheath (red) bonded to (a) a modified saliva ejector, or (b) a modified disposable dental mirror. Insets show cross-sections of the imaging portion of the catheter holders showing the 0.9mm OD catheter within the 1.5mm OD sheath. Relative to the orientation in the insets, the catheters are pressed downwards against the tissue. (c,d) Photographs of the catheter holders in use.

In the clinical setting, the open-ended catheters were inserted into a 1.5 mm OD, water-filled, clean, single-use, closed-ended plastic sheath. For easily accessible areas, the bare sheath was held in place by hand. More often, however, imaging was performed using the sheath attached to one of two catheter sheath holder designs (Fig. 2). The objective of designing catheter sheath holders was to allow single-handed placement of the imaging catheter with sufficient stability to maintain tissue contact without motion while also minimally obstructing the clinician's view of the imaging area. The first probe holder design was based on a standard clear saliva ejector (Fig. 2(a)). The strainer tip was removed and the plastic tube was cut back to leave approximately 90 mm of plastic-covered copper forming wire protruding. The catheter sheath was inserted into the uncut portion of the saliva ejector tube and affixed to the wire protrusion using cyanoacrylate adhesive. Due to the ability to form the shape of the tip of this catheter sheath holder prior to imaging, this design allowed easy placement of the imaging catheter in restrictive areas of the oral cavity such as the floor of the mouth and the gingiva. The second catheter sheath holder was based on a disposable dental mirror with the adhesive mirror removed (Fig. 2(b)). A shallow groove was cut onto the bottom surface of the mirror and the catheter sheath was adhesively bonded to the groove and along the handle. This design was well suited to placement of the catheter on relatively expansive planar areas such as the tongue and buccal mucosa. Photos of the two catheter sheath holders in use are shown in Fig. 2(c)-2(d). For the bare sheath and the modified saliva ejector catheter holder design, the full 90mm imaging length is possible. Due to its size, the imaging length for the modified dental mirror catheter holder design is restricted to less than 40mm.

#236612 Received 20 Mar 2015; revised 18 Jun 2015; accepted 19 Jun 2015; published 24 Jun 2015

For *in vivo* imaging of oral lesions an imaging (pullback) axis was chosen; usually along the longest extent of the lesion. Pullback speeds of 2-4 mm/s at 100 Hz rotational rates were used yielding 20 – 40 micrometer resolution along the pullback axis and imaging times to a maximum of 45 s for the full 90 mm pullback. Imaging times for smaller lesions were shorter accordingly.

Polarization sensitive images were produced using the Jones matrix formalism published previously by Wang *et al* [31] and presented as retardation images with a color map spanning 0 to π. The reflection from the interface between the catheter sheath outer surface and the tissue was used as the reference surface defined to have zero retardation. Detailed analysis and imaging validation with this system have been explored in a previous manuscript [32].

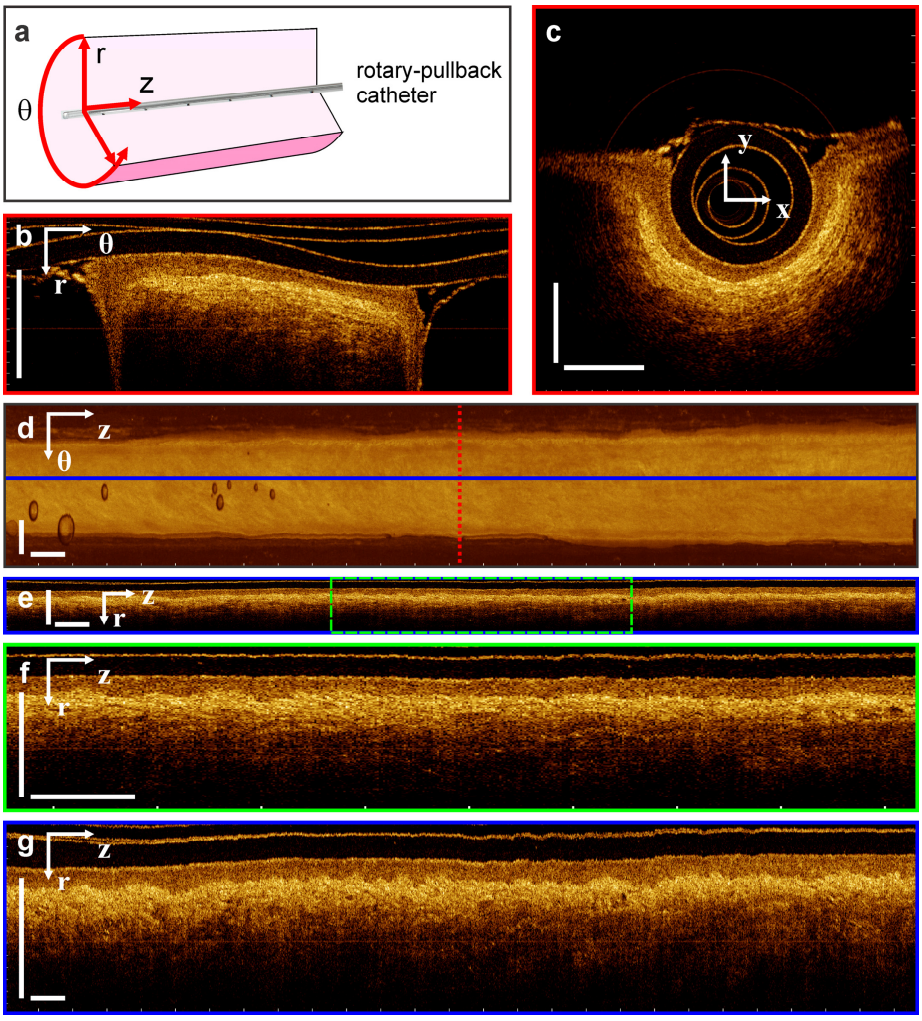

Fig. 3. Wide-field OCT data presentation of a 27 mm pullback (pullback speed = 2 mm/s) of normal lateral tongue from a 59-year old male subject taken with the modified dental mirror catheter sheath holder. The pullback direction is from left to right. (a) Rotary pullback catheter coordinate system. (b) Polar and (c) Cartesian presentations of a single imaging frame indicated by dashed (red) line in the *en face* projection shown in (d). (e,g) Azimuthal presentation along solid (blue) line in (d). (f) Zoomed azimuthal view of dashed (green) box in (e). The aspect ratio in (e) and (f) is 1:1 while (g) has been stretched vertically to show more detail. White bars in the images are 1 mm in length. The θ axes in the images have been scaled as if the image has been projected onto the outer diameter of the 1.5 mm catheter sheath. There is no averaging for these images, $w = 1$.

#236612 Received 20 Mar 2015; revised 18 Jun 2015; accepted 19 Jun 2015; published 24 Jun 2015

3. Results

To date, we have collected 176 *in vivo* OCT volumes from 51 patients. The imaged areas included lesions ranging from dysplasia to squamous cell carcinoma, as well as premalignant lesions and scars from previously resected oral cancer. Where possible, normal mucosa contralateral to the lesions were also imaged. Overall, the OCT acquisition procedure was well tolerated by the patients and only added 2-3 minutes to clinical visit times. No discomfort was reported with the catheter sheath or either of the catheter sheath holders.

Examples of data collected are presented in Fig. 3–6. In Fig. 3, we show a 27 mm pullback collected at 2 mm/s from the clinically normal lateral tongue of a 59-year old male subject. The acquired OCT volumes have cylindrical symmetry with radial (r), azimuthal (θ), and pullback (z) axes as shown in Fig. 3(a). Data is collected as frames in the polar r-θ coordinate system (Fig. 3(b)). The imaging depth penetration into tissue is approximately 1 mm while the θ coordinate spans one complete rotation of the catheter optics. By coordinate transformation, the polar images can viewed as Cartesian x-y images (Fig. 3(c)) where the tissue wraparound on the catheter sheath outer diameter can be easily seen. The non-circular appearance of the 0.9mm OD catheter and 1.5mm OD catheter sheath in the Cartesion presentations in Fig. 3–6 is due to deformation of these plastic components and the lack of a mechanism to maintain their concentricity. A (pseudo-) *en face* projection can display the entire data set as a single θ-z image by averaging the volume over the radial (r) coordinate (Fig. 3(d)). We note that the *en face* label is a misnomer as θ is an angular coordinate. In the *en face* projection, we label the θ axis with a linear dimension as if the image is projected onto the surface of the 1.5 mm OD catheter sheath, making the full extent of the *en face* image 4.71 mm. Figure 3(e) shows a two-dimensional azimuthal (r-z) slice of the volumetric OCT data in one-to-one aspect ratio (i.e. equal scaling along the r and z axes). A zoom of a segment of the azimuthal slice is displayed in Fig. 3(f) to show more detail. The entire azimuthal slice can be easily viewed in a single panel by stretching the r axis scaling compared to the z axis as shown in Fig. 3(g). This latter type of azimuthal presentation is used for the remainder of this work.

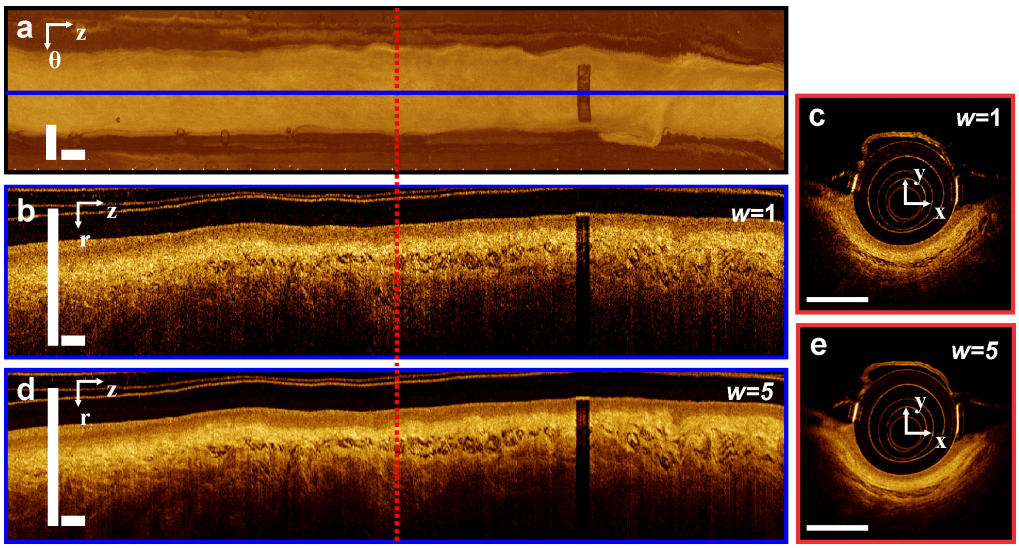

Fig. 4. OCT image of clinically normal lateral tongue from a 58-year old female subject acquired with the modified dental mirror catheter sheath holder. The pullback direction is from left to right. (a) *En face* projection displaying 33mm x 4.7mm FOV. (b,d) Azimuthal views along solid (blue) line shown in (a). (c,e) Cartesian views along dotted (red) line shown in (a). (b,c) have no averaging, w = 1 (d,e) have been averaged with a triangular kernel of width 5, w = 5. The white bars in the images are 1 mm in length. The theta scale bar in (a) has been scaled as if image is projected onto outer diameter of catheter sheath.

#236612 Received 20 Mar 2015; revised 18 Jun 2015; accepted 19 Jun 2015; published 24 Jun 2015

Speckle in the Cartesian and azimuthal views can be reduced by averaging adjacent sections in the orthogonal z and θ directions, respectively at the cost of reduced spatial resolution. We have used a triangular averaging kernel of full width w for the averaged images presented following. Figure 4 shows a 33 mm pullback segment collected at 4 mm/s cropped from the complete pullback of a clinically normal lateral tongue of a 58-year old female subject. The azimuthal FOV has a width of approximately 180 degrees, corresponding to a linear width of about 2.3 mm at the 1.5 mm OD of the catheter sheath. The black rectangle visible in the image is a black reference marker printed on the catheter sheath. Figure 4(b) and Fig. 4(c) show azimuthal and Cartesian views along the solid (blue) and dotted (red) lines indicated in Fig. 4(a), respectively. Figure 4(b) and Fig. 4(c) have not been averaged along the orthogonal directions (w = 1). As has been reported previously, a lightly scattering (signal sparse) epithelium is separated by the basement membrane and lies atop a more heavily scattering submucosa. Figures 4(d) and 4(e) show the same azimuthal and Cartesian views as Fig. 4(b) and Fig. 4(c) except with a triangular averaging kernel of w = 5 applied. This kernel width corresponds to 3.6 degrees and 0.2 mm in the azimuthal and pullback directions, respectively. This inter-frame averaging leads to marked reduction in the image speckle at the cost of slightly reduced resolution in the orthogonal direction. Along the pullback axis, the continuity of the basement membrane, relatively constant thickness of the epithelium, and regular patterning of the submucosa, all indicative of normal oral tissue, can be quickly ascertained from the averaged azimuthal image.

Figure 5 shows OCT imaging of a clinically visible white lesion (Fig. 5(b)) from the contralateral tongue surface of the same subject as described in Fig. 4. Readily apparent in the *en face* projection (Fig. 5(a)) is a dark region labeled L. Azimuthal and Cartesian slices through L shown in Fig. 5(c) and Fig. 5(d), respectively, show thickening of the epithelium, loss of visibility of the basement membrane, and loss of normal submucosal tissue structure around L, comparing to those from the normal looking mucosa on the right side of Fig. 5(c) and the contralateral location (Fig. 4(d) and Fig. 4(e)).

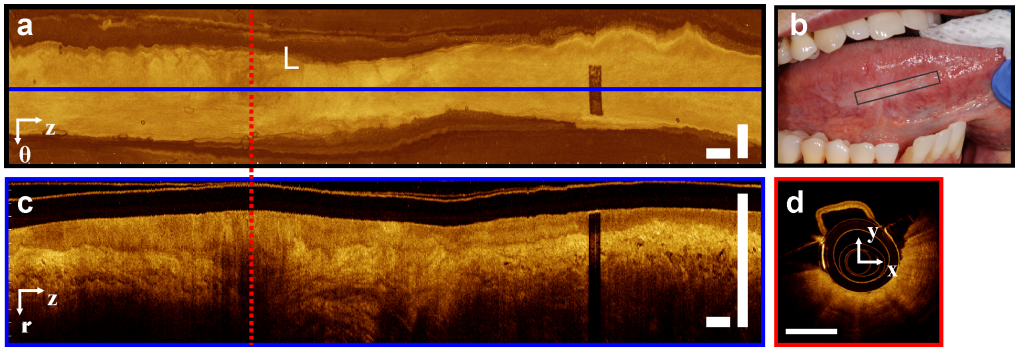

Fig. 5. OCT image of clinically visible lesion from same subject as Fig. 4 contralateral to the previous imaging location. The pullback direction is from left to right. (a) *En face* projection displaying 33mm x 4.7mm FOV. L indicates a dark region. (b) Clinical photo of lesion and approximate imaging location (c) azimuthal view along solid (blue) line shown in (a). (d) Cartesian view along dotted (red) line shown in (a). The white bars in the images are 1 mm in length. The images are averaged with a triangular kernel of width 5, w = 5.

In Fig. 6, PSOCT imaging of an oral submucosal fibrosis lesion on the buccal mucosa of a 48-year-old male patient is shown. The most distal marking on the catheter sheath (leftmost in Fig. 6(a)) was placed on the clinically visible posterior edge of the lesion. The extent of the clinically visible lesion along the imaging axis was measured for comparison with imaging and is indicated by a pair of solid (pink) vertical lines in the *en face* projection and azimuthal slices (Figs. 6(a), 6(c), 6(f)). The *en face* image (Fig. 6(a)) is unremarkable except for some irregular vertical patterning near the right boundary of the lesion which likely coincides with the anterior boundary of the lesion. This boundary is about 2mm away from that denoted by the pink line and gives an indication of the precision of matching the clinical perception with

#236612 Received 20 Mar 2015; revised 18 Jun 2015; accepted 19 Jun 2015; published 24 Jun 2015

the OCT imaging location. The azimuthal presentation along the solid (blue) horizontal line (Fig. 6(c)) shows an abnormal and very corrugated epithelial-submucosal boundary. The corresponding azimuthal retardation image (Fig. 6(f)) shows tight horizontal banding in the lesion region (i.e. between the pink lines), indicating high birefringence due to the underlying fibrotic tissue. Outside of the lesional area, there is less birefringence. This is further demonstrated in the structural OCT and retardation Cartesian slices along the dotted (red) and dashed (green) lines (Figs. 6(d)-6(e), 6(g)-6(h)). Parasitic back-reflections within the catheter result in imaging artifacts: straight horizontal lines in the azimuthal view (Fig. 6(c)); and perfect circles centered on the origin in the Cartesian views (Fig. 6(d) and 6(e)).

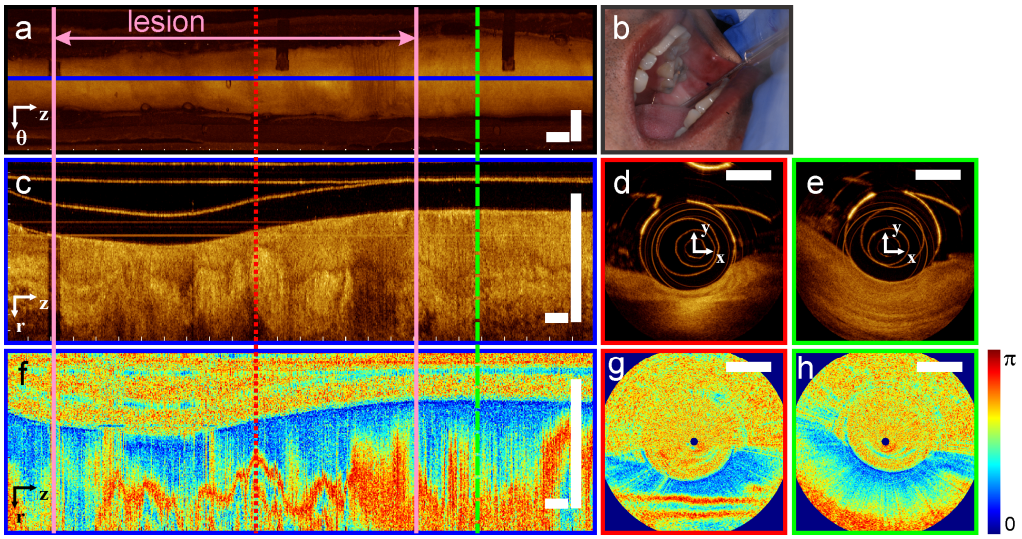

Fig. 6. OCT imaging of a submucosal fibrosis lesion on the buccal mucosa of a 48-year old male patient. The pullback direction is from left to right corresponding to posterior to anterior orientation. (b) Clinical photo of the lesion being imaged with the modified saliva ejector catheter holder. Structural OCT (a) *en face* projection and (c) azimuthal slice. The clinically visible lesion is indicated between the solid (pink) vertical lines. Slices along the dotted (red) and dashed (green) lines are shown in Cartesian images in (d) and (e) respectively. (f, g, h) Retardation images corresponding to the structural images (c,d,e) respectively. The images are averaged with a triangular kernel of width 5, w = 5. The white bars in the images are 1 mm in length.

4. Discussion

We have designed and developed a hand-held *in vivo* OCT device that is able to generate volumetric imaging data within seconds during a single acquisition from oral mucosal surfaces. With large FOV and easily positioned fast rotary pullback catheters, this system has overcome limitations of previously demonstrated oral OCT probes. The large FOV is desirable for clinical usage since it eliminates the need for the clinician to manually scan over the tissue when using small FOV probes, thus eliminating the possibility that diagnostically important tissue areas are missed. It also obviates the need to stitch small FOVs together to create larger FOVs. The actual time required to acquire an OCT pullback is determined by the pullback speed and the length of the pullback. Slower pullbacks provide higher *z* resolution at the expense of increased scanning time, which may become an issue if patient or clinician motion is problematic. Thus, the optimal imaging speed that balances *z* resolution and scan time depends on the clinical situation. In our setting, we were able to obtain high quality images using 2-4 mm/s pullbacks with 100 Hz rotational rates.

The 1.5 mm OD disposable catheter sheath serves multiple purposes. First, it is a cost-effective way for eliminating the possibility of cross-contamination between patients, obviating the need to reprocess the relatively expensive and delicate imaging catheter. It also

#236612 Received 20 Mar 2015; revised 18 Jun 2015; accepted 19 Jun 2015; published 24 Jun 2015

provides a method for quick changeover between patients, which is important if this tool is to be used as a screening tool. Finally, the sheath extends the tissue surface away from the catheter axis, thus creating a longer arc length along the circumference against which the tissue rests. Assuming that the catheter images over a 180 degree arc, the effective FOV in the θ dimension with the 1.5 mm OD catheter sheath is 2.4 mm, compared to only 1.4 mm for the 0.9 mm OD catheter alone. This increase in FOV comes at the expense of decreased lateral resolution in the θ dimension which scales linearly with the distance from the catheter axis. The optimal compromise between lateral resolution and FOV in the θ dimension for RPCs is determined by the image quality required for the desired application. As demonstrated here, visualizing basement membrane continuity and epithelial thickness does not require high lateral resolution and the wider increased θ FOV is desirable for covering larger lesions.

Image volumes generated by RPCs are long and skinny but have a significant advantage over comparable linear fiber scanners driven back and forth along the catheter axis because the ability to average along the θ coordinate in the azimuthal views gives much greater image quality with reduced speckle. With high quality, large FOV azimuthal images produced by this instrument, histological features important for cancer diagnosis reported previously [15, 33] such as basement membrane continuity, keratinization, epithelial thickening, broadening of rete pegs, irregular epithelial stratification, and basal hyperplasia, can be now be analyzed over long continuous distances. For example, as seen in Fig. 4 and Fig. 5, it is easy to see if continuity of the basement membrane is preserved, and if not, exactly where and over what distance it is missing.

While it has been established that OCT imaging of the oral mucosa has the potential to play a role in the clinical decision making process, in the absence of large, statistically powerful studies that show high sensitivity and specificity, it is unlikely that OCT imaging alone will replace conventional biopsy in the short term. A more forthcoming clinical application is to reduce the number of biopsies needed from large lesions with an improvement in the diagnostic representational accuracy of these biopsies, through effective biopsy guidance using OCT imaging. The *en face* view presented here is particularly useful for quickly visualizing the entire data set. In Fig. 5, the darker region that indicates a loss of basement membrane is easily identified for further examination. Although the averaging functionality has not yet been implemented in the current data acquisition software, all of the views are readily available to the clinician immediately after acquisition. Being able to view and evaluate the data set immediately and quickly is important for OCT to be used for point-of-care biopsy site selection.

Pre-operatively, wide-field OCT visualization of basement membrane continuity to recognize superficially invasive cancer could be extremely important for tumor staging and determining proper disease management. Additionally, analysis of imaging features may be useful for more accurately delineating tumors pre-operatively to reduce morbidity, mortality, and cost associated with disease recurrence. Currently, fluorescence visualization [34] has shown promise for this application, but is still somewhat subjective and can be misleading in some cases such as when hyperkeratinization is present.

PSOCT is able to image the birefringence of highly ordered tissues such as muscle and collagen [35]. As shown in Fig. 6, PSOCT readily shows the birefringence of the fibrotic submucosa of this precancerous lesion. Further studies are necessary to explore whether this non-invasive imaging method can be used to monitor progression of these lesions towards cancer or to monitor therapeutic treatments. Additionally, by differentiating collagen-containing scar tissue from mucosa, PSOCT may be useful for monitoring disease recurrence near surgical margins of previously resected oral cancers. The PSOCT implementation used here may be sub-optimal for maximum birefringence sensitivity compared to those that use couplers with lower polarization mode dispersion [36] and sequential orthogonal Poincare representation incident polarizations [37]. However, besides being simple to use and inexpensive to construct compared to PSOCT implementations using active polarization modulation, the system presented here has higher power throughput to the tissue than those

#236612 Received 20 Mar 2015; revised 18 Jun 2015; accepted 19 Jun 2015; published 24 Jun 2015

using couplers. This feature is important as losses through the FORJ and RPCs are relatively high.

Doppler OCT is another imaging extension that has been used with RPCs to map vasculature in the lung [29] and other organs. Although possible with this OCT instrument, the necessary slow scanning parameters are difficult to realize without motion artifacts due to the handheld imaging catheter. Another limitation of using RPCs for tissue imaging is the contact nature of the probe that can lead to tissue compression which may distort the tissue from its natural state. However, any type of imaging access to lesion sites in the oral cavity usually involves manual manipulation of the tongue, lips, and cheeks that stretches the tissue away from its natural rest state.

In conclusion, we demonstrate an *in vivo* wide-field oral cavity polarization-sensitive OCT imaging system that uses rotary pullback catheters. This system rapidly generates tissue volumetric data sets up to 2.5 x 90 mm^2 in size in seconds. We have developed catheter sheaths and holders that allow easy placement of the catheter at any site within the oral cavity. These high-quality wide-field images allow evaluation of tissue features over dimensions not previously demonstrated *in vivo*. Wide-field and rapid imaging, and versatile catheter placement within the oral cavity make this OCT system favorable for clinical usage.

Acknowledgments

The authors would like to thank Dr. Samson Ng, Dr. Donald Anderson, Tony Han, Alisa Kami, and Grace Manaog for clinical assistance. This work was supported by a Collaborative Health Research Projects grant from the Canadian Institutes of Health Research (CIHR) and Natural Sciences and Engineering Research Council of Canada (NSERC).